PHYSICAL REVIEW B **83**, 184402 (2011)

Epitaxial growth and ferrimagnetic behavior of $MnFe_2O_4(111)$ ultrathin layers for room-temperature spin filtering

S. Matzen,[1] J.-B. Moussy,[1] R. Mattana,[2] K. Bouzehouane,[2] C. Deranlot,[2] F. Petroff,[2] J. C. Cezar,[3] M.-A. Arrio,[4] Ph. Sainctavit,[4] C. Gatel,[5] B. Warot-Fonrose,[5] and Y. Zheng[6]
[1]*CEA-Saclay, IRAMIS, SPCSI, F-91191 Gif-Sur-Yvette, France*
[2]*Unité Mixte de Physique CNRS/Thales, F-91767 Palaiseau, France, and University of Paris-Sud 11, F-91405 Orsay, France*
[3]*ESRF, F-38043 Grenoble, France*
[4]*IMPMC, F-75015 Paris, France*
[5]*CEMES-CNRS, F-31055 Toulouse, France*
[6]*INSP, CNRS UMR7588, F-75015 Paris, France*

(Received 22 December 2010; published 9 May 2011)

We report on the epitaxial growth and physical properties of spinel $MnFe_2O_4(111)$ thin films with thicknesses down to 2 nm. The thin films, grown on α-$Al_2O_3(0001)$ single crystals or Pt(111) buffer layers by oxygen-assisted molecular beam epitaxy, exhibit high structural order with sharp interfaces and low roughness. The electrical and magnetic properties are carefully investigated and it is shown that $MnFe_2O_4(111)$ ultrathin films keep an insulating and ferrimagnetic behavior at room temperature. Special attention is given to the iron/manganese valence state and the cationic ordering. X-ray absorption spectroscopy and magnetic circular dichroism measurements reveal that thin films contain mainly Fe^{3+} and Mn^{2+} cations, distributed predominantly in a normal spinel structure. This study proves the high potential of $MnFe_2O_4$ to be used as a magnetic tunnel barrier for spin filtering applications at room temperature.

DOI: 10.1103/PhysRevB.83.184402 PACS number(s): 75.70.−i, 75.25.−j, 85.75.−d, 75.47.Lx

I. INTRODUCTION

The generation of highly spin-polarized currents is one of the critical technologies for developing high performance spintronics devices such as magnetic random access memories and spin metal-oxide-semiconductor field-effect transistors. In the last few years, spin filters, constituted by a ferromagnetic or ferrimagnetic tunnel barrier, have emerged as a promising alternative to create artificial spin-polarized current sources. Ferromagnetic spin filters rely on the spin-dependent transmittance of ferromagnetic tunnel barriers due to the existence of an exchange-split band gap. Spin filtering at room temperature could potentially impact future generations of spin-based device technologies,[1] not only because spin filters may function with 100% efficiency[2] but also because they can be combined with any nonmagnetic metallic electrode, thus providing a versatile alternative to half-metals or MgO-based classic tunnel junctions.

Following the pioneering work of Moodera *et al.*,[3] who showed spin filtering at low temperature using EuS ferromagnetic tunnel barriers with a Curie temperature (T_c) around 16 K, spin filtering has been demonstrated using oxide barriers, such as EuO (Ref. 4) ($T_c = 69$ K), perovskite oxides[5] ($BiMnO_3$, $T_c = 105$ K), and, more recently, spinel oxides or ferrites barriers: $NiFe_2O_4$ (Ref. 6) ($T_c = 850$ K) and $CoFe_2O_4$ (Refs. 7–10) ($T_c = 793$ K). As the Curie temperature of ferrites is well above room temperature, efficient room-temperature spin-polarized sources could be obtained using these oxides. However, room-temperature spin filtering has only been reported in $CoFe_2O_4$-based tunnel junctions[8,10] due to the difficulty of fabricating room-temperature ferrimagnetic barriers.

Manganese ferrite oxide ($MnFe_2O_4$) is another exciting and promising candidate for room-temperature spin-filter applications. Until now, $MnFe_2O_4$ films have essentially been grown by pulsed laser deposition at thicknesses above 100 nm for microwave applications. Toward this goal, the ability to enhance magnetic anisotropy in $MnFe_2O_4$ films has been investigated by using alternating-target laser ablation deposition technique in order to tune the cation distribution and tailor the magnetic properties of manganese ferrites.[11,12] The Mn substitution to Fe_3O_4 has also been studied for controlling properties such as carrier concentration and magnetism in highly conductive thin films, and Ishikawa *et al.*[13] have successfully prepared low-resistance and spin-polarized Mn-doped Fe_3O_4 thin films at room temperature. $MnFe_2O_4$ is considered to be predominantly of the normal spinel structure, as about 80% of tetrahedral sites are populated by Mn^{2+} ions.[14] It exhibits insulating properties with a small gap[15] and has a low magnetocrystalline anisotropy constant (K_1) at room temperature ($K_1 = -33.10^3$ erg/cm^3) corresponding to an anisotropic field (H_a) of 175 Oe.[16] Thanks to its insulating properties and high Curie temperature ($T_c = 573$ K), $MnFe_2O_4$ could act also as a spin filter at room temperature if the film still exhibits the required physical properties when its thickness is reduced to a tunnel barrier thickness (e.g., a few nanometers). As its predicted spin decomposed exchange splitting of the conduction bands[15] is higher (3.85 eV) than for the inverse $NiFe_2O_4$ (1.21 eV) and $CoFe_2O_4$ (1.28 eV) spinel oxides, $MnFe_2O_4$ could lead to better spin-filtering efficiencies.

In this paper, we study the potential of $MnFe_2O_4$ to be used as a magnetic tunnel barrier in spin-filter-based magnetic tunnel junctions. We report on the epitaxial growth of $MnFe_2O_4(111)$ ultrathin films, using oxygen-assisted molecular beam epitaxy (MBE). A number of *in situ* and *ex situ* characterization techniques have been used to optimize the growth in order to obtain epitaxial ultrathin films with excellent structural and chemical properties. Then, a careful study of the electrical and magnetic properties has been made with special attention given to the iron/manganese cationic ordering showing that $MnFe_2O_4(111)$ ultrathin films have a huge potential to be used as room-temperature magnetic tunnel barriers for spin-filtering applications.

II. EXPERIMENT

The $MnFe_2O_4(111)$ thin films have been grown by oxygen-assisted MBE following a procedure inspired by the previously optimized growth of $Fe_3O_4(111)$ (Ref. 17) and $CoFe_2O_4(111)$ (Ref. 18) on α-$Al_2O_3(0001)$ substrates with or without a Pt(111) underlayer. Manganese ferrites were deposited at 450 °C with a radio frequency oxygen plasma source operated during the metal (Fe and Mn) evaporation in an ultrahigh vacuum (UHV) chamber with an oxygen partial pressure of 10^{-8} mbar during deposition. The system allowed for the real-time observation of the structural evolution by *in situ* reflection high-energy electron diffraction (RHEED), as well as postdeposition verification of the iron and manganese oxidation states in the ferrite films by *in situ* x-ray photoemission spectroscopy (XPS).

The bulk structure of thin films was characterized *ex situ* by x-ray diffraction (XRD) using the Cu $K_{\alpha 1}$ radiation in the 2θ range from 5° to 85°. X-ray reflectivity (XRR) and atomic force microscopy (AFM) have also been used to measure the films thicknesses and root-mean-square (rms) roughnesses. A study by transmission electron microscopy (TEM) has also been performed, allowing us to describe the structure of the films in both conventional and high-resolution [high-resolution transmission electron microscopy (HRTEM)] modes using a Tecnai F20 fitted with a spherical aberration corrector (point resolution = 0.12 nm). The cross-sectional specimens for TEM studies were cut along the $(11\bar{2})$ spinel planes before thinning by tripod grinding and ion milling to achieve the electron transparency.

The electrical properties of the $MnFe_2O_4(111)$ layers grown on a Pt(111) underlayer (20 nm thick) were probed with a conductive tip atomic force microscope (CT-AFM).[19] Resistance mappings of 20 μm × 20 μm regions were collected, by applying a bias voltage of 1 V, at room temperature with a 10^{-12}–10^{-4} A current range and Si_3N_4 tips coated with B-doped diamond.

The magnetic behavior of thin films has been investigated using a vibrating sample magnetometer (VSM) at room temperature with a magnetic field applied up to 2 T or using a VSM-PPMS (physical properties measurement system) setup from room temperature down to liquid helium with a magnetic field up to 7 T. The majority of the measurements were performed with the magnetic field aligned parallel to the film surface. However, perpendicular geometry measurements were also taken to check the anisotropy in the films.

In order to access the cationic sites' distribution, the valence, and the specific magnetic properties of *3d* elements (Fe and Mn) in our $MnFe_2O_4$ ultrathin films, we performed x-ray absorption spectroscopy (XAS) and x-ray magnetic circular dichroism (XMCD) experiments at the Mn and Fe $L_{2,3}$ edges at room temperature at the ID08 beamline of the European Synchrotron Radiation Facility (ESRF). Samples were exposed to a magnetic field of 5 T applied perpendicular to the sample surface and parallel to the wave vector of incoming photons. XAS and XMCD spectra were recorded at 300 K by using the circularly polarized light with the degree of circular polarization almost 100% in the total electron yield (TEY) mode. The XMCD spectra were taken switching both the circular polarization helicity of the x-rays and the orientation of the magnetic field in order to minimize any systematic drift. The base pressure of the system was around 5×10^{-10} Torr. The total resolution for XAS was less than 100 meV, while that for XMCD was about 120 meV at the Mn $L_{2,3}$ and Fe $L_{2,3}$ edges.

III. RESULTS AND DISCUSSION

A. Structural and chemical characterizations

The magnetism in ferrite thin films has been shown to be very sensitive to effects such as strain[20] and stoichiometry,[13] while the structure and chemistry at the interfaces in spin-filter-based tunnel junctions are also known to play a crucial role in the spin-filtering efficiency. Our structural study therefore began with *in situ* RHEED analyses performed in real time throughout the deposition process. The RHEED patterns were studied along the $[10\bar{1}0]$ and $[1\bar{1}00]$ directions based in the hexagonal real space of the α-$Al_2O_3(0001)$ substrate. Figure 1 shows the RHEED patterns along both observation directions of a $MnFe_2O_4$ (5 nm) ultrathin layer grown on top of a buffer layer of Pt (20 nm). Immediately after placing the buffer layer into the flow of metal (Fe, Mn) and oxygen, smooth streaks corresponding to the (0,1)- and (1,1)-type planes of the face-centered-cubic (fcc) sublattice are observed, indicating that the film growth is two dimensional as of its initial stages. Intermediate (0, 3/2) and (1/2, 1/2) streaks next appear after about 10 min, corresponding to a film thickness of about 1 nm and revealing the characteristic RHEED patterns of the spinel structure. These intermediate streaks persist and intensify throughout the entire duration of the deposition, indicating that the desired spinel phase is maintained and that the growth mode remains two dimensional. We have controlled the $MnFe_2O_4$ growth mode until thicknesses up to 50 nm. A study of the spacing between the streaks in the RHEED patterns of $MnFe_2O_4$ films show that our films are fully relaxed from 1.2 nm thick (i.e., under no mechanical strain due to the α-Al_2O_3 or Pt interface).

The control of the composition of our $MnFe_2O_4(111)$ ultrathin films was performed using *in situ* XPS, with an Al K_α source. We have focused our attention on the Fe $2p$ and Mn $2p$ peaks in the XPS spectra, as is shown in Fig. 2 for a $MnFe_2O_4$(5 nm) layer. In the case of the Fe $2p$ spectrum of $MnFe_2O_4$, the presence of Fe^{3+} cations yields a well-defined structure 8 eV after the Fe $2p_{3/2}$ peak (711 eV), whereas in Fe_3O_4 this peak is smeared out due to the presence of both Fe^{2+} and Fe^{3+} in almost equal proportion.[21] The shape of the Mn $2p$ also signals the presence of Mn^{2+} rather than another oxidation state. Figure 2 shows the Mn $2p$ electron binding-energy spectrum which consists of spin-orbit-split $2p_{3/2}$ and $2p_{1/2}$ peaks. These two peaks are very close to those of the $2p_{3/2}$ and $2p_{1/2}$ states of MnO ($2p_{3/2} \sim 640.6$ and $2p_{1/2} \sim 652.2$ eV).[22] Furthermore, we observe the formation of shake-up satellites, which are offset from the main peaks of the Mn $2p$ doublet

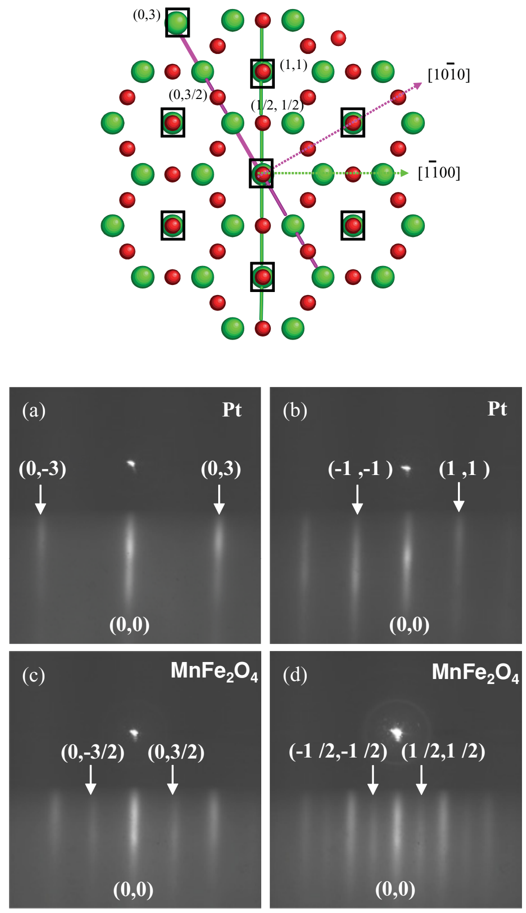

FIG. 1. (Color online) Top: Schemating reciprocal lattices of α-Al$_2$O$_3$(0001) (large green circle), Pt(111) (square), and MnFe$_2$O$_4$(111) (small red circle). Bottom: RHEED patterns of the Pt(111) underlayer (a,b) and a 5-nm MnFe$_2$O$_4$(111) thin film (c,d) observed along the [10$\bar{1}$0] (left column) and [1$\bar{1}$00] (right column) directions.

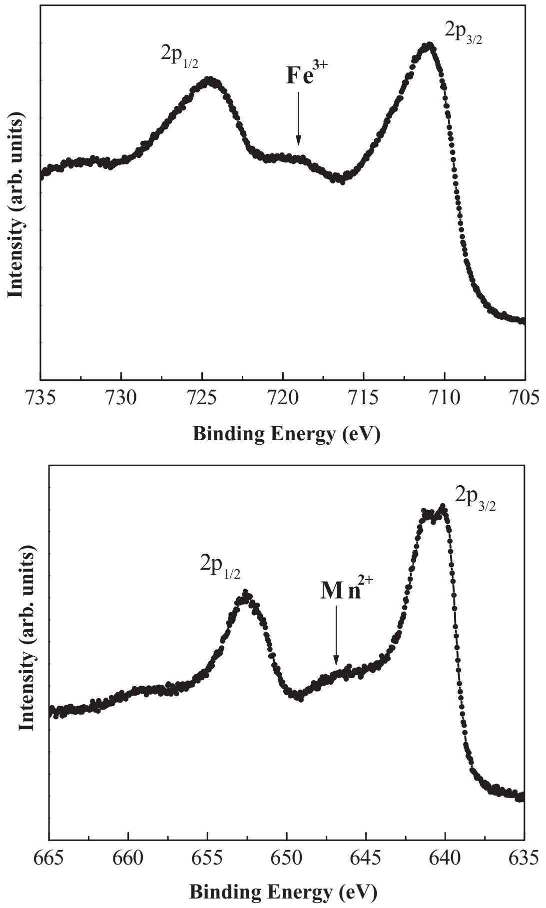

FIG. 2. Fe $2p$ and Mn $2p$ XPS spectra of an α-Al$_2$O$_3$/MnFe$_2$O$_4$ (5 nm) thin film.

by approximately 5 eV toward higher binding energies. This behavior is typical for Mn^{2+} systems.[23,24] In summary, the development of the Mn $2p$ doublet provides clear evidence for the presence of Mn^{2+} ions.

However, from the Mn $2p$ signal, we cannot exclude any presence of Mn^{3+}. Indeed, it is seen that the $2p_{3/2}$ peak is split by two lines with the energy difference of 1 eV. This could verify the multivalence character of Mn ions, due to Mn^{2+} ($\sim$ 640 eV) and Mn^{3+} ($\sim$ 641 eV) ions,[25] often observed in manganite thin films. As many groups[24] have questioned the suitability of the Mn $2p$ signal for investigations of the Mn valence, we performed XAS and XMCD experiments to access more precisely the valence and the cationic sites' distribution in our MnFe$_2$O$_4$ ultrathin films (see Sec. III C). By comparing the Fe $2p$ and Mn $2p$ peak intensities, we were also able to quantify the Mn/Fe ratio in our films. In all cases, we obtained the correct stoichiometry within the accuracy limit of the XPS method, which is within 10% of the expected 1/2 ratio.

Ex situ characterization of the MnFe$_2$O$_4$ (15 nm) thin layers has been done by XRD [Fig. 3(a)]. At first, only 111-type reflections were observed, confirming the unidirectional growth by MBE and excluding the possible existence of parasitic phases. The rocking curves obtained on the (222) peaks have a full-width at half-maximum (FWHM) of 0.05° for films of 15 nm, showing the high texture of the layers. The out-of-plane cell parameter c is 0.8513 nm, comparable to the bulk cell parameter. X-ray reflectivity measurements [Fig. 3(b)] additionally allowed us to check the film thicknesses predicted from the calibration of the atomic fluxes. We successfully fitted the periodicity of the reflectivity oscillations to find thicknesses that agree with the expected values. These measurements gave also another indication of the very low films roughness, as had already been seen on the RHEED patterns. A typical x-ray reflectivity curve is shown in Fig. 3(b), with the parameters of the fit (SLD is the scattering length density obtained). A low rms surface roughness of 0.2 nm was also determined using an AFM in tapping mode for a MnFe$_2$O$_4$(5 nm) layer [Fig. 3(c)]. This remarkably low value lends itself very well to the growth of more complex epitaxial heterostructures, such as future magnetic tunnel junctions.

The microstructure of MnFe$_2$O$_4$ ultrathin films was studied by high- and low-resolution TEM over a significant portion of each of the films along the [11$\bar{2}$] zone axis. Figure 4(a) shows a low-magnification micrograph of a 5-nm-thick MnFe$_2$O$_4$ film on its α-Al$_2$O$_3$(0001) substrate. This image demonstrates the homogeneity and the smoothness of the layer across a large portion of substrate surface. Figure 4(b) shows the typical HRTEM micrograph of a 5-nm-thick MnFe$_2$O$_4$ film.

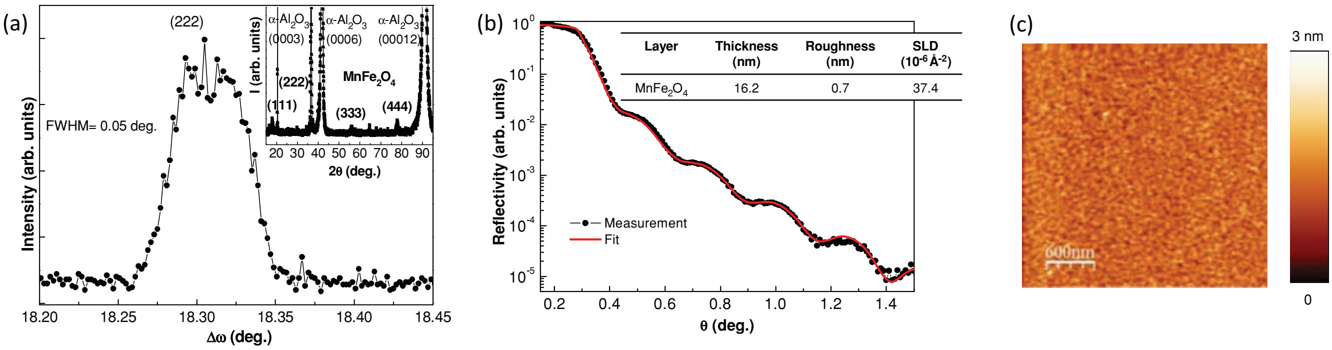

Layer	Thickness (nm)	Roughness (nm)	SLD (10^{-6} Å^{-2})
$MnFe_2O_4$	16.2	0.7	37.4

FIG. 3. (Color online) (a) Rocking curve of the (222) peak for a 15-nm-thick $MnFe_2O_4(111)$ film grown on α-Al_2O_3. The typical XRD pattern is shown in the inset. (b) X-ray reflectivity of an α-$Al_2O_3/MnFe_2O_4$ thin film with the associated fit table. (c) AFM image (3 μm × 3 μm) of an α-$Al_2O_3/MnFe_2O_4$ (5 nm) thin film.

In this image, we clearly identify the (111) planes of Mn and Fe cations oriented parallel to the substrate surface. The homogeneity and high structural quality of the oxide layer is evident with an α-$Al_2O_3(0001)/MnFe_2O_4(111)$ interface which is perfectly flat and abrupt. There is no trace of parasitic phases resulting from the formation of unwanted (Fe, Mn) oxides during the early stages of film growth. These observations are in good agreement with the real-time RHEED diffraction patterns in which a single-phase and two-dimensional growth mode is observed as soon as the oxide begins to form.

Figure 5(a) shows the strain map along the growth direction. This image has been calculated from the HRTEM micrograph using the geometric phase analysis (GPA) method.[26] The deformation value on the $MnFe_2O_4$ layer compared to the substrate is equal to 14%, very close to the expected theoretical value (13.5%) in considering the (111) plane for $MnFe_2O_4$ and the (0006) plane for Al_2O_3. This result confirms the fully relaxed state of the ferrite layer. The stress relaxation is due to the network of misfit dislocations clearly visible on the amplitude image obtained by GPA [Fig. 5(b)]: these dislocations coming from the large misfit between the ferrite layer and the substrate are regularly-spaced and confirm the relaxed state, in good agreement with our previous RHEED and XRD characterizations. No epitaxial strain will therefore modify the magnetic properties of the films.

Finally, Fig. 4(b) evidences the presence of one of the most common defects known to appear in epitaxial ferrite thin films: the antiphase boundaries (APBs). These APBs have been observed on all HRTEM micrographs recorded on this sample indicating a huge density of these defects.

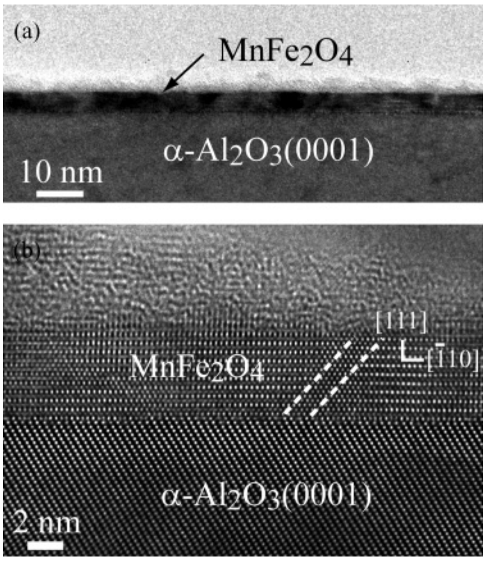

FIG. 4. Cross-sectional TEM images of a $MnFe_2O_4$ (5 nm) film viewed along the [11$\bar{2}$] zone axis. (a) Low magnification image. (b) High magnification image. The presence of a tilted APB has been labeled by white dashed lines.

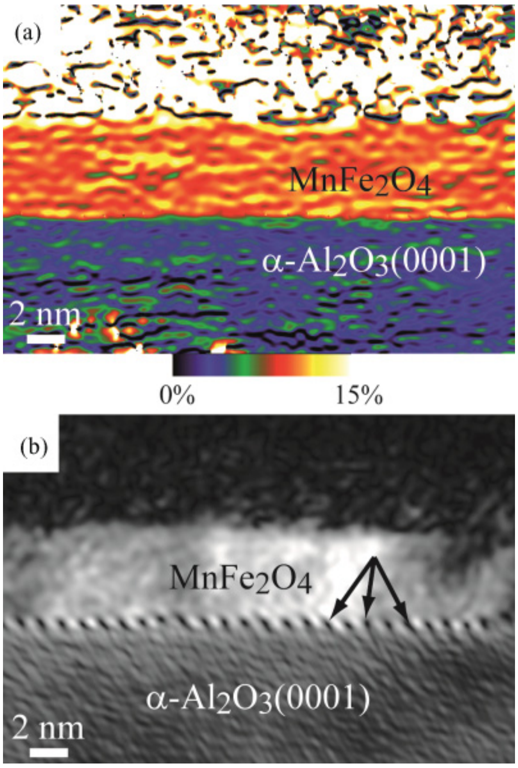

FIG. 5. (Color online) (a) Strain map along the growth direction calculated from the HRTEM image using the GPA method. (b) Amplitude image with regularly spaced constrasts (some of them are indicated by arrows) corresponding to the misfit dislocations.

APBs are stacking defects of the atomic planes in the spinel lattice corresponding to a half-lattice translation of the cationic sublattice, whereas the oxygen sublattice remains unchanged. In the case of Fe_3O_4, these APBs have been widely studied due to their important effect on the magnetic[17,27] and magnetotransport[28–30] properties of this material. In the case of $MnFe_2O_4$, much less is known. Nevertheless, it is clear that APBs are an important factor to keep in mind when interpreting future magnetic (Sec. III C) and spin-polarized transport measurements.

B. Electrical properties

To be used as tunnel barriers, our $MnFe_2O_4$ ultrathin films have to exhibit insulating properties. Thus, we have measured their electrical properties using a CT-AFM. As $CoFe_2O_4$ tunnel barriers have shown spin-filtering capabilities at room temperature, we have used a $CoFe_2O_4$ (5 nm) film as a reference to compare with our $MnFe_2O_4$ ultrathin films. Figure 6 shows a typical resistance mapping of a 3 μm × 3 μm region on an α-Al_2O_3/Pt(20 nm)/$CoFe_2O_4$ (5 nm) reference, with an average resistance (R_{avg}) of $\log R_{avg} = 7.2 \pm 0.2$. $MnFe_2O_4$ films have been characterized and a typical resistance mapping of a 20 μm × 20 μm region on an α-Al_2O_3/Pt (20 nm)/$MnFe_2O_4$ (5 nm) reference is shown in Fig. 6. Our $MnFe_2O_4$ ultrathin films are highly homogeneous, without hot spots or pin holes on 20 × 20 μm^2 surfaces. They are insulating with an average resistance (R_{avg}) 4 orders of magnitude higher than that for the Pt buffer [$\log R_{avg} = 8.2 \pm 0.2$ for the $MnFe_2O_4$ (5 nm) film]. So the resistivity of $MnFe_2O_4$ ultrathin films is even higher than that for $CoFe_2O_4$ tunnel barriers (Fig. 6). Furthermore, I-V curves have been measured (insets of Fig. 6) and present a nonlinear shape, which is characteristic of the expected tunneling behavior. Consequently, $MnFe_2O_4$ ultrathin films show adequate properties to be used as tunnel barriers and to allow electrons tunneling through micrometer-scale magnetic tunnel junctions.

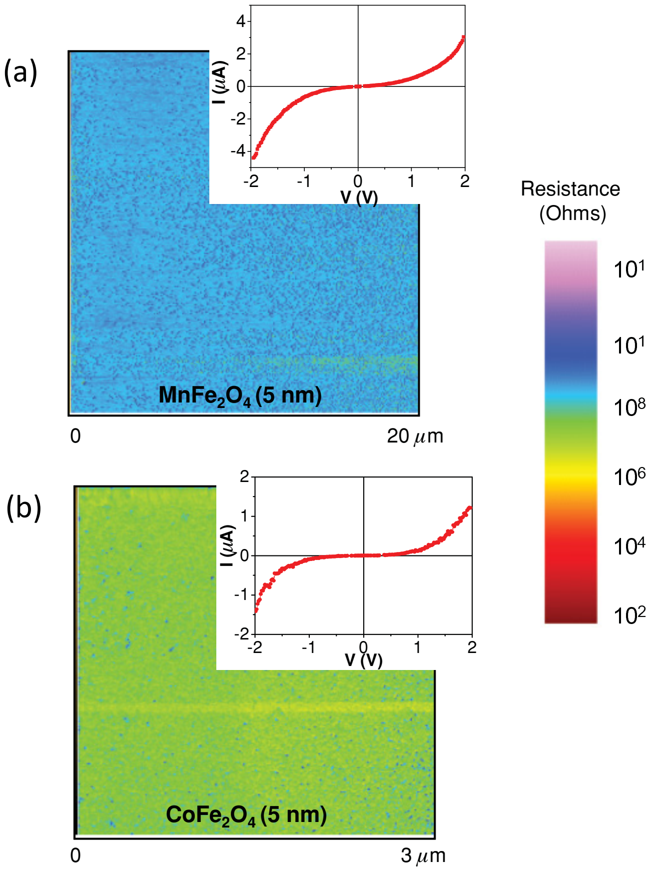

FIG. 6. (Color online) (a) Resistance surface map (20 μm × 20 μm) for an α-Al_2O_3/Pt (20 nm)/$MnFe_2O_4$ (5 nm) layer, showing its highly insulating and homogeneous properties. (b) Resistance surface map (3 μm × 3 μm) for an α-Al_2O_3/Pt (20 nm)/$CoFe_2O_4$(5 nm) reference layer. (Insets) I-V curves measured for both layers.

C. Magnetic properties and cationic distribution

The magnetism in $MnFe_2O_4$ thin films for thicknesses varying from 50 nm to thicknesses appropriate for tunnel barriers (2–5 nm) was studied by VSM. In all magnetic hysteresis loops presented here, the diamagnetic contribution from the substrate was subtracted. Both in-plane and out-of-plane measurements were performed confirming a magnetic easy axis in the plane of the films, as expected due to shape anisotropy. Within the in-plane measurements, we also checked for any planar angular anisotropy, which proved to be insignificant (not shown here). This agrees with the lack of angular dependence found in Fe_3O_4 epitaxial films with a (111) orientation.[17]

The in-plane magnetic hysteresis loops of typical 50-, 15-, and 5-nm $MnFe_2O_4$ layers obtained at room temperature are shown in Fig. 7(a). The 50-nm film hysteresis loop exhibits a net magnetization of 280 kA/m or a magnetic moment (μ) of 2.3 μ_B per formula unit (f.u.) at high field, a coercive field (H_c) of 145 Oe, and a remanent magnetization of 76%. When decreasing the thickness from 50 to 5 nm, one observes a decrease of both magnetization at high field and remanence which is typical of ferrite thin films. The 5 nm ultrathin films still clearly show an open hysteresis loop with a net magnetization of 200 kA/m ($\mu = 1.7\ \mu_B$/f.u.) at high field and 10% of remanence. The coercivity $H_c = 60$ Oe is also smaller than the one observed in the thick layers. This observation is consistent with the natural increased presence of antiphase boundaries in the thinner films (which have been observed in our $MnFe_2O_4$ films by TEM), as these structural defects are known to be in part responsible for the decreased coercivity in ferrite thin films.[17,18] $MnFe_2O_4$ ultrathin films were also grown on top of an epitaxial Pt(111) buffer layer deposited on the sapphire substrate. In this case [shown in Fig. 7(b)], the 5-nm-thick films have typically a coercivity around 170 Oe with a magnetization of 350 kA/m ($\mu = 3\ \mu_B$/f.u.) and a remanence of 25%, much greater than that of equivalent films grown without a Pt buffer layer. We note that all of the samples that we compared were aligned identically with respect to the applied magnetic field in order to exclude deceiving geometry effects on the measured magnetic signal. The effect of the Pt buffer has been observed repeatedly and is likely tied to the quicker spinel phase formation and higher intensity RHEED patterns observed during the growth of these films. The reduction of certain defects such as misfit dislocations

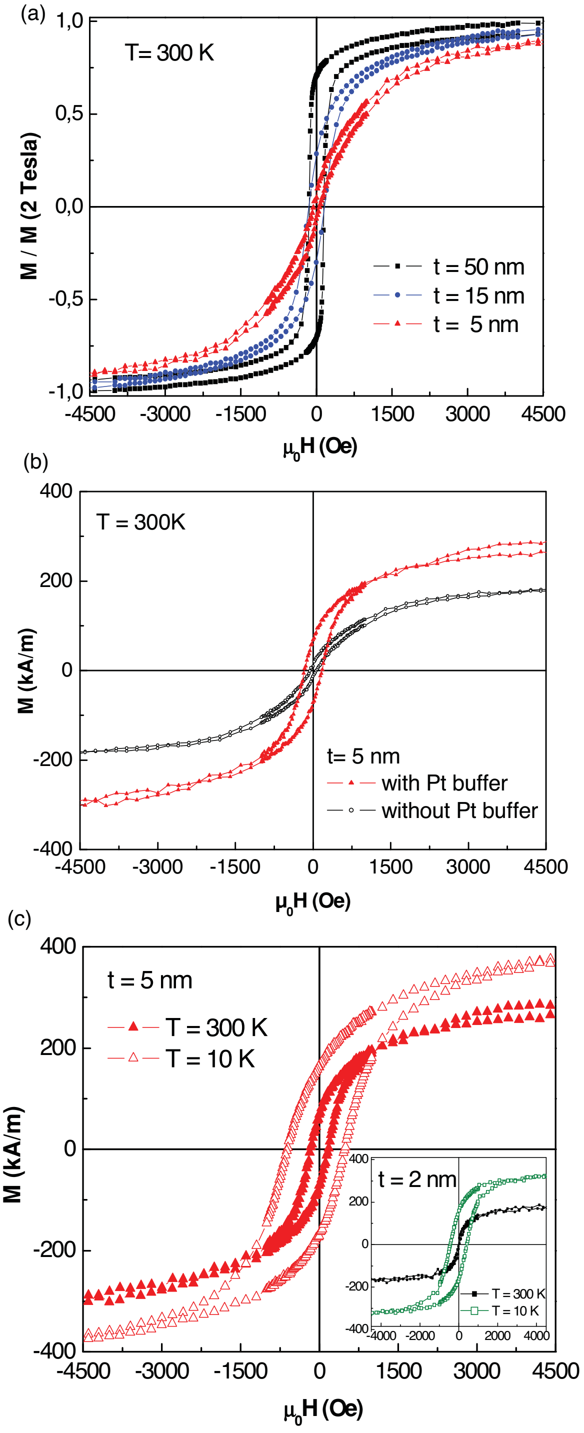

FIG. 7. (Color online) (a) In-plane magnetic hysteresis loops for α-Al_2O_3/$MnFe_2O_4$(111) thin films (50, 15, and 5 nm) at T = 300 K. (b) In-plane magnetic hysteresis loops for an α-Al_2O_3/$MnFe_2O_4$(111) (5 nm) thin film and an α-Al_2O_3/Pt(20 nm)/MnF_2O_4(111) (5 nm) thin film at T = 300 K. (c) In-plane magnetic hysteresis loops for an α-Al_2O_3/Pt(20 nm)/$MnFe_2O_4$ (111) (5 nm) (2 nm, in inset) thin film at T = 300 K and 10 K.

and APBs in the Pt-based layers may very well improve the magnetic order in the $MnFe_2O_4$ films, leading to the improved coercivity and magnetic moment. By using the Pt buffer, the thickness of the films can be reduced until 2 nm, while keeping an open hysteresis loop ($H_c = 20$ Oe at 300 K) [inset of Fig. 7(c)].

In-plane hysteresis loops of typical 5- and 2-nm-thick $MnFe_2O_4$(111) films grown on Pt(111) have also been studied at room and low temperatures [Fig. 7(c)]. One can verify that the low-temperature magnetization curves do not present any unpleasant surprises with respect to the room-temperature characterization. These magnetization loops indicate that the coercivity and remanence are somewhat affected by the drop in temperature, increasing to 550 Oe and 40%, respectively, in comparison to the 170 Oe and 25% values obtained at room temperature for a 5-nm-thick $MnFe_2O_4$(111) film. The increase in remanence is obviously beneficial for future tunneling experiments. The increase in coercivity is related to the anisotropy constant increase while decreasing temperature. In conclusion, these measurements clearly show that our $MnFe_2O_4$ films still conserve a very good magnetic character at room temperature when the thickness is reduced to a tunnel barrier thickness.

The most important chemical information, missing from the *in situ* XPS experiments, is the interstitial site distribution of Mn and Fe cations. The site distribution is a particularly crucial point to consider in the case of future $MnFe_2O_4$ spin-filter tunnel barriers because electronic band structure calculations predict that the band gap and the exchange splitting in the conduction band change significantly when passing from the inverse to the normal spinel structure,[15] that is, when the Mn^{2+} cations go from octahedral to tetrahedral sites. Each of these parameters is a determinant factor for the spin-filter characteristics of this material.

In order to access the cationic sites' distribution in our $MnFe_2O_4$ ultrathin films, we performed XAS and XMCD experiments at the ESRF synchrotron light source. XAS[31,32] and XMCD[33,34] are indeed powerful experimental tools for studying the valence and magnetic moment per atom of transition metal ions in solids and their distribution between octahedral and tetrahedral sites.

XMCD studies have been previously reported for polycrystalline $MnFe_2O_4$ powders[35] and nanocrystalline thick films of $Mn_xFe_{3-x}O_4$ (150-nm sputtered films[36] and 100-nm films obtained by pulsed laser deposition[24]). Our experiments are thus the first ones on epitaxial $MnFe_2O_4$ ultrathin films. We present here an analysis of the Fe $L_{2,3}$ and Mn $L_{2,3}$ spectra, allowing us to identify the valence states of Mn and Fe ions and their interstitial site placement. These XAS and XMCD experiments have been performed on five ultrathin layers and have shown similar spectra.

Figure 8 shows the Fe and Mn $L_{2,3}$ edges' XAS and XMCD spectra obtained for a $MnFe_2O_4$ (5 nm) film deposited on α-Al_2O_3 with a Pt(111) buffer layer. The spectra were recorded in the total electron yield mode, which has a probing depth of around 5 nm, allowing us to probe the main part of the $MnFe_2O_4$ layer. These spectra show the multiplet structure, typical of the ionic nature of iron and manganese. Fe and Mn XMCD spectra [Figs. 8(b) and 8(d)] are mostly of opposite sign, suggesting that the magnetic moments of Fe and Mn have an antiparallel orientation. In the spinel structure, there is a ferrimagnetic order with an antiparallel alignment between magnetic moments in tetrahedral (T_d) and octahedral (O_h) sites. Thus, this first look at the experimental data is consistent

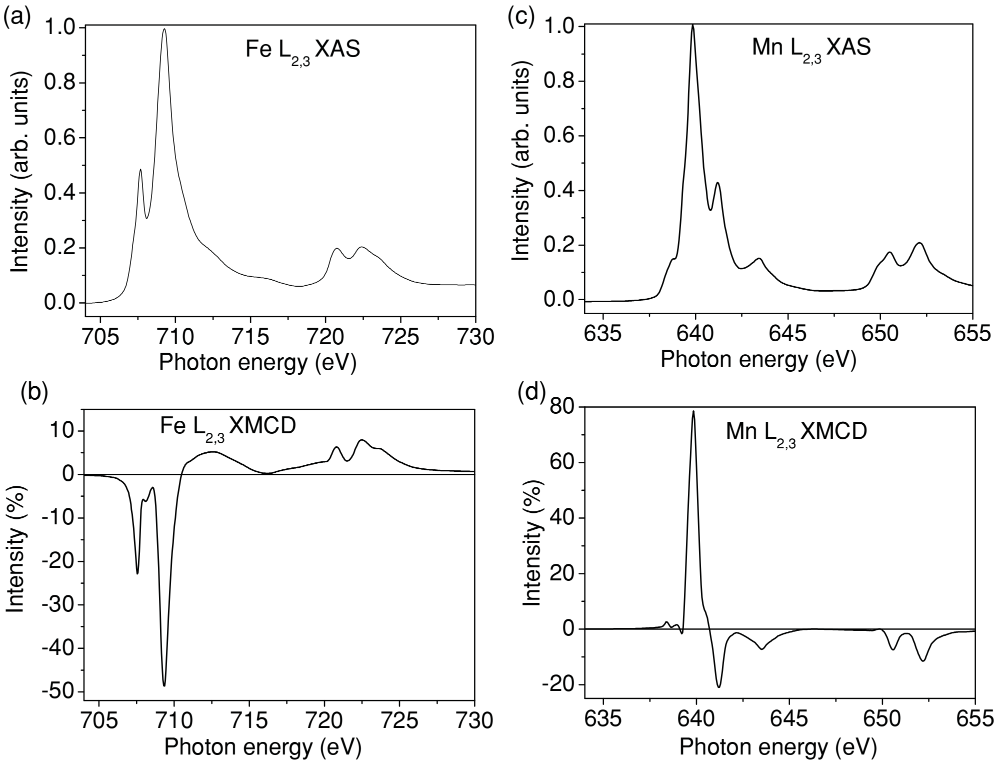

FIG. 8. Fe and Mn $L_{2,3}$ edges' XAS and XMCD spectra obtained for a $MnFe_2O_4$ (5 nm) film deposited on α-Al_2O_3 with a Pt(111) buffer layer (T = 300 K, H = ±5 T).

with a ferrimagnetic order in our $MnFe_2O_4$ films. It shows that the Mn (respectively Fe) atoms occupy mostly the tetrahedral (respectively octahedral) sites, which seems coherent with a normal-type spinel structure.

XAS and XMCD spectra of transition-metal oxides often show the multiplet structures, and their line shapes are strongly dependent on the occupied *3d* electron configurations, the crystal field, the spin-orbit and electron-electron interactions within the transition metal atom, and the hybridization of *3d* electrons to other valence electrons. Taking into account these facts, each specific contribution of Mn and Fe (for a given valence and site position) can be calculated using a crystal field atomic multiplets approach, and then the overall XAS and XMCD spectra can be obtained for a chosen cationic distribution of different species. Here the calculated spectra have been obtained by employing the ligand-field multiplet (LFM) model[37] by including the spin-orbit interaction between $3d$ electrons with the magnetic field along the (111) direction of the spinel structure.

In Fig. 9(a), we have compared the measured Mn $L_{2,3}$ edges' XAS spectrum of $MnFe_2O_4$ to the calculated Mn $L_{2,3}$ edges' XAS spectra, obtained from the LFM calculations using the following crystal field splitting parameter values (10 Dq). The three calculated XAS spectra (blue lines) represent those for Mn^{2+} ($3d^5$) under O_h with 10 Dq = 1.2 eV, Mn^{2+} ($3d^5$) under T_d with 10 Dq = 0.5 eV, and Mn^{3+} ($3d^4$) under O_h with 10 Dq = 1.2 eV. This comparison reveals clearly that Mn ions in $MnFe_2O_4$ are nearly divalent and occupy essentially tetrahedral sites. The best fit is obtained (particularly for the "A" feature) for a weighted sum of [20% Mn^{2+} (O_h) + 80% Mn^{2+} (T_d)] (red line). In Fig. 9(b), we have also compared the measured Mn $L_{2,3}$ edges' XMCD spectra of $MnFe_2O_4$ to the calculated ones. The Mn $L_{2,3}$ XMCD spectrum of $MnFe_2O_4$ is also qualitatively similar to that of Mn^{2+} (T_d), and we can see a good correspondence between the measurement and the calculation (red line). The spinel structure of $MnFe_2O_4$ can be described by the formula $[Mn_{1-y}Fe_y]_{T_d}[Fe_{2-y}Mn_y]_{O_h}O_4$, where y is called the inversion parameter. The inversion parameter is known to vary from 0 to 0.2 for bulk $MnFe_2O_4$, among which 0.2 is the most usual, but the cation distribution was found to be sensitive to the processing oxygen pressure and the preparation technique,[38] and a higher inversion parameter can be obtained in thin films. Thus, concerning the Mn ions, our $MnFe_2O_4$ thin films contain mainly Mn^{2+} cations in tetrahedral sites, with an estimated inversion parameter ($y = 0.2$) corresponding to the reported bulk value. Furthermore we can notice that the XAS and XMCD spectra for Mn^{3+} are at higher energies compared with the ones for the 2+ valence. So we can exclude the presence of manganese 3+ in our films, which was questioned by our XPS measurements.

In Fig. 10(a), we have compared the measured Fe $L_{2,3}$ edges' XAS spectrum of $MnFe_2O_4$ to the calculated Fe $L_{2,3}$ XAS spectra. The three calculated XAS spectra (blue lines) represent those for Fe^{3+} ($3d^5$) under O_h with 10 Dq = 1.5 eV, Fe^{3+} ($3d^5$) under T_d with 10 Dq = 0.7 eV, and Fe^{2+} ($3d^6$) under O_h with 10 Dq = 1.4 eV[39]. By comparing the experimental XAS data with calculated spectra, we immediately see a close resemblance with the Fe^{3+} (O_h) XAS line shape, indicating that the valence state of Fe ions in $MnFe_2O_4$ is mainly trivalent. In Fig. 10(b), we have compared the measured Fe

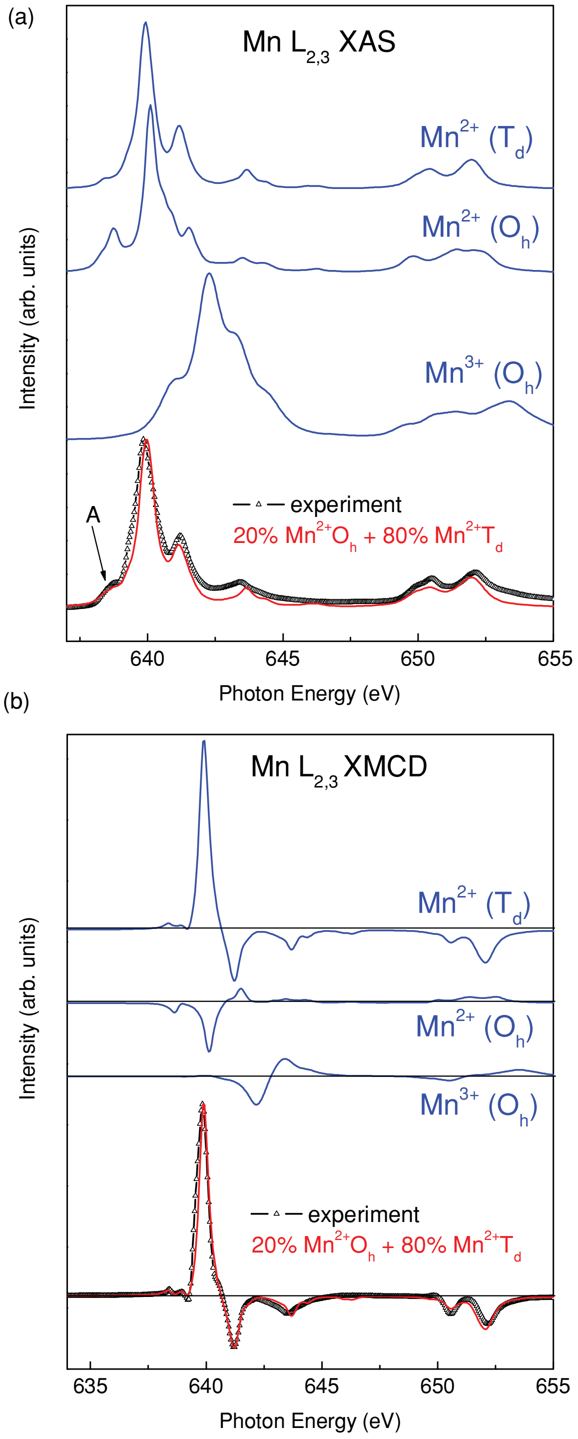

FIG. 9. (Color online) Comparison of the Mn $L_{2,3}$ edges' XAS (a) and XMCD (b) of $MnFe_2O_4$ (5 nm) to the calculated Mn $L_{2,3}$ edges' XAS (a) and XMCD (b) for Mn^{2+} (T_d), Mn^{2+} (O_h), and Mn^{3+} (O_h) (blue lines) and their weighted sum (red line) (T = 300 K, H = ±5 T).

$L_{2,3}$ XMCD spectrum of $MnFe_2O_4$ to the calculated Fe $L_{2,3}$ XMCD spectra. The Fe $L_{2,3}$ XMCD spectrum of $MnFe_2O_4$ is also qualitatively similar to that of Fe^{3+} (O_h), but the difference in the feature "B" seems to indicate that Fe ions in $MnFe_2O_4$ occupy not only O_h sites but also T_d sites. First, we have compared the measured Fe XAS and XMCD spectra to the calculated spectra obtained for a weighted sum of [10% Fe^{3+} (T_d) + 90% Fe^{3+} (O_h)] (red lines), giving an inversion parameter of 0.2 for Fe ions. A reasonably good agreement is found between experiment and calculation, and is comparable to previous results for $MnFe_2O_4$ powders[35] and nanocrystalline thick films.[36] We can further improve the agreement with the experimental data by introducing more tetrahedral Fe^{3+} and a

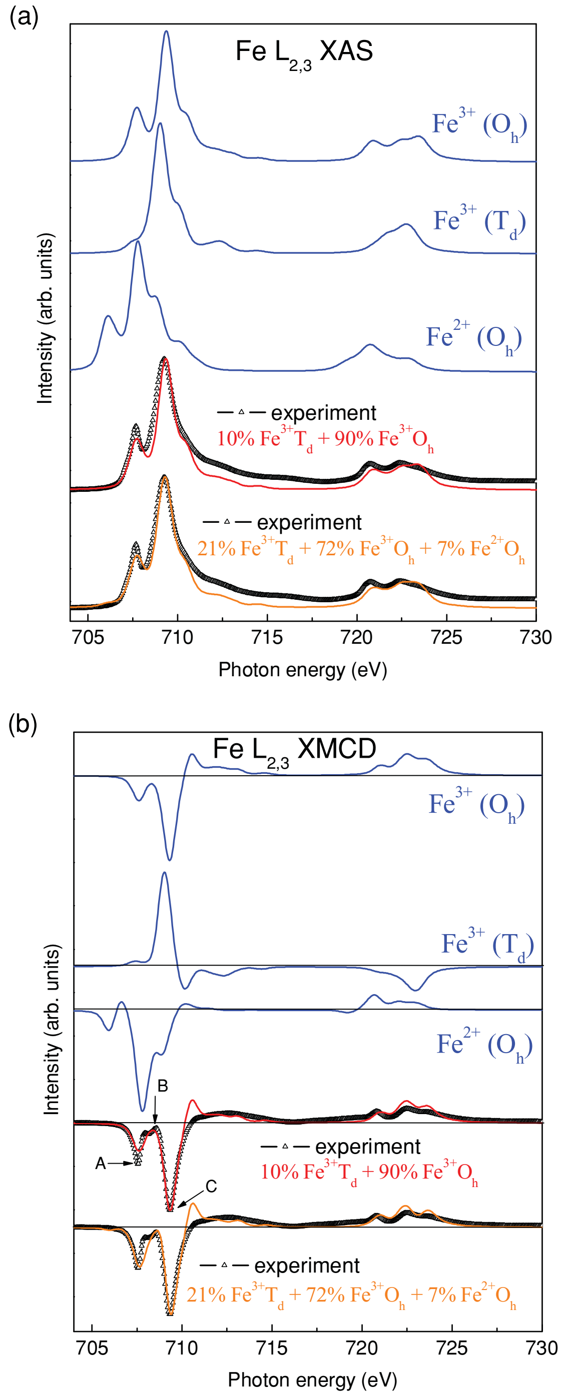

FIG. 10. (Color online) Comparison of the Fe $L_{2,3}$ edges' XAS (a) and XMCD (b) of $MnFe_2O_4$ (5 nm) to the calculated Fe $L_{2,3}$ edges' XAS (a) and XMCD (b) for Fe^{3+} (O_h), Fe^{3+} (T_d), and Fe^{2+} (O_h) (blue lines) and their weighted sum (red and orange lines) (T = 300 K, H = ±5 T).

small fraction of divalent Fe ions to get the right ratio between peaks A, B, and C. The orange curve in Fig. 10(b) represents the weighted sum of 21% Fe^{3+} (T_d) + 72% Fe^{3+} (O_h) + 7% Fe^{2+} (O_h), describing the best fit with the measured Fe $L_{2,3}$ XMCD spectrum. The XAS spectrum is also calculated for this weighted sum and compared to the Fe $L_{2,3}$ XAS spectrum in Fig. 10(a) (orange line). At this point, we can say that our $MnFe_2O_4$ thin films contain mainly Fe^{3+} cations, with an inversion parameter probably higher than 0.2 ($y = 0.42$) for the Fe ions' distribution. Concerning the Mn ions' distribution, we have also noticed that the calculated spectra do not change significantly for an inversion parameter of 0.4. Consequently, from the quality of fitting, our $MnFe_2O_4$ ultrathin films can be described by mainly Fe^{3+} cations, with an inversion parameter probably higher than 0.2, and by Mn^{2+} cations distributed either with the same inversion parameter or with the 0.2 bulk value (suggesting that some octahedral sites should be unoccupied). Thus, our $MnFe_2O_4$ ultrathin films have a slightly higher inversion than usual reported spinel structures of $MnFe_2O_4$ powders (inversion of 20%).[35] This could be due to the high density of APBs which modify the cationic stacking and thus the cationic environment in ultrathin films.

To conclude, these XAS and XMCD measurements have revealed the rather normal spinel structure of our $MnFe_2O_4$ ultrathin films. This structure will be further very beneficial for spin-filtering efficiency since the normal structure is predicted to show a higher spin decomposed exchange splitting of the conduction bands (3.85 eV) than for the inverse structure (1.31 eV).[15] This important determination of the cationic site distribution will be extremely valuable for future interpretation of the spin-filter characteristics of our $MnFe_2O_4$ tunnel barriers.

IV. CONCLUSION

In this paper, we have reported on the epitaxial growth of ultrathin manganese ferrite films (2–5 nm in thickness), using oxygen-assisted MBE. A two-dimensional and single phase growth mode has been successfully optimized to get the desired spinel structure of $MnFe_2O_4$(111) without any parasitic phase and with a very low surface roughness. Our RHEED, XRD, and HRTEM measurements have clearly revealed the excellent structural quality of our manganese ferrite ultrathin films, and their composition has been controlled by *in situ* XPS to get the correct stoichiometry and oxidation states. The films have then been characterized electrically and show adequate properties (highly insulating behavior without pin holes on large surfaces) to be used as tunnel barriers. Finally, thanks to an in-depth magnetic study, we have proved that $MnFe_2O_4$ films keep a ferrimagnetic behavior until tunnel barrier thicknesses at room temperature. XAS and XMCD experiments have also allowed us to access the cationic sites' distribution in manganese ferrite ultrathin films, which contain mainly Fe^{3+} and Mn^{2+} cations, distributed predominantly as in a normal spinel structure. This structure is predicted to exhibit good spin-filter characteristics and thus the epitaxial $MnFe_2O_4$ ultrathin films are very promising to be used as ferrimagnetic tunnel barriers operating at room temperature. We are presently integrating these spinel oxides in $MnFe_2O_4$-based spin-filter tunnel junctions in order to conduct spin-polarized transport measurements.

ACKNOWLEDGMENTS

This work has been supported by the C'nano IdF and the RTRA-Triangle de la Physique under grants FILASPIN and MicMMaC, respectively.

---

[1] J. S Moodera, T. S Santos, and T. Nagahama, J. Phys. Condens. Matter **19**, 165202 (2007).

[2] J. S Moodera, R. Meservey, and X. Hao, Phys. Rev. Lett. **70**, 853 (1993).

[3] J. S Moodera, X. Hao, G. A Gibson, and R. Meservey, Phys. Rev. Lett. **61**, 637 (1988).

[4] T. S Santos and J. S Moodera, Phys. Rev. B **69**, 241203 (2004).

[5] M. Gajek, M. Bibes, A. Barthélémy, K. Bouzehouane, S. Fusil, M. Varela, J. Fontcuberta, and A. Fert, Phys. Rev. B **72**, 020406 (2005).

[6] U. Luders, M. Bibes, K. Bouzehouane, E. Jacquet, J.-P. Contour, S. Fusil, J. Fontcuberta, A. Barthélémy, and A. Fert, Appl. Phys. Lett. **88**, 082505 (2006).

[7] M. G. Chapline and S. X. Wang, Phys. Rev. B **74**, 014418 (2006).

[8] A. V. Ramos, M.-J. Guittet, J.-B. Moussy, R. Mattana, C. Deranlot, F. Petroff, and C. Gatel, Appl. Phys. Lett. **91**, 122107 (2007).

[9] A. V. Ramos, T. S Santos, G. X. Miao, M.-J. Guittet, J.-B. Moussy, and J. S Moodera, Phys. Rev. B. **78**, 180402(R) (2008).

[10] Y. K. Takahashi, S. Kasai, T. Furubayashi, S. Mitani, K. Inomata, and K. Hono, Appl. Phys. Lett. **96**, 072512 (2010).

[11] X. Zuo, A. Yang, S. D. Yoon, J. A. Christodoulides, V. G. Harris, and C. Vittoria, Appl. Phys. Lett. **87**, 152505 (2005).

[12] A. Yang, Z. Chen, A. L. Geiler, X. Zuo, D. Haskel, E. Kravtsov, C. Vittoria, and V. G. Harris, Appl. Phys. Lett. **93**, 052504 (2008).

[13] M. Ishikawa, H. Tanaka, and T. Kawai, Appl. Phys. Lett. **86**, 222504 (2005).

[14] J. M. Hastings and L. M Corliss, Phys. Rev. **104**, 328 (1956).

[15] Z. Szotek, W. M. Temmerman, D. Kodderitzsch, A. Svane, L. Petit, and H. Winter, Phys. Rev. B **74**, 174431 (2006).

[16] J. Smith and H. P. J. Wijn, *Ferrites* (Wiley, New York, 1959), Chap. VIII, p. 163.

[17] J.-B. Moussy, S. Gota, A., Bataille, M.-J. Guittet, M. Gautier-Soyer, F. Delille, B. Dieny, F. Ott, T. D. Doan *et al.*, Phys. Rev. B **70**, 174448 (2004).

[18] A. V. Ramos, J.-B. Moussy, M.-J. Guittet, M. Gautier-Soyer, C. Gatel, P. Bayle-Guillemaud, B. Warot-Fonrose, and E. Snoeck, Phys. Rev. B **75**, 224421 (2007).

[19] F. Houzé, R. Meyer, O. Schneegans, and L. Boyer, Appl. Phys. Lett. **69**, 1975 (1996).

[20] Y. Suzuki, R. B. van Dover, E. M. Gyorgy, J. M. Phillips, V. Korenivski, D. J. Werder, C. H. Chen, R. J. Cava, J. J. Krajewski, W. F. Peck, and K. B. Do, Appl. Phys. Lett. **68**, 714 (1996).

[21] S. Gota, E. Guiot, M. Henriot, and M. Gautier-Soyer, Phys. Rev. B **60**, 14387 (1999).

[22] J. Gao, S. Y. Dai, and T. K. Li, Phys. Rev. B **67**, 153403 (2003).

[23] E. Beyreuther, S. Grafström, L. M. Eng, C. Thiele, and K. Dörr, Phys. Rev. B **73**, 155425 (2006).

[24] J. Takaobushi, M. Ishikawa, S. Ueda, E. Ikenaga, J. J. Kim, M. Kobata, Y. Takeda, Y. Saitoh, M. Yabashi, Y. Nishino, D. Miwa, K. Tamasaku, T. Ishikawa, I. Satoh, H. Tanaka, K. Kobayashi, and T. Kawai, Phys. Rev. B **76**, 205108 (2007).

[25] K. J. Kim, H. J. Lee, and J. Y. Park, J. Magn. Magn. Mater. **321**, 3706 (2009).

[26] M. J. Hÿtch, E. Snoeck, and R. Kilaas, Ultramicroscopy **74**, 131 (1998).

[27] D. T. Margulies, F. T. Parker, M. L. Rudee, F. E. Spada, J. N. Chapman, P. R. Aitchison, and A. E. Berkowitz, Phys. Rev. Lett. **79**, 5162 (1997).

[28] M. Ziese and H. J. Blythe, J. Phys. Condens. Matter **12**, 13 (2000).

[29] W. Eerenstein, T. T. M. Palstra, S. S. Saxena, and T. Hibma, Phys. Rev. Lett. **88**, 247204 (2002).

[30] A. V. Ramos, J. B. Moussy, M. J. Guittet, A. M. Bataille, M. Gautier-Soyer, M. Viret, C. Gatel, P. Bayle-Guillemaud, and E. Snoeck, J. Appl. Phys. **100**, 103902 (2006).

[31] F. M. F. de Groot, J. C. Fuggle, B. T. Thole, and G. A. Sawatzky, Phys. Rev. B **42**, 5459 (1990).

[32] S. C. Wi, J.-S. Kang, J. H. Kim, S.-B. Cho, B. J. Kim, S. Yoon, B. J. Suh, S. W. Han, K. H. Kim, K. J. Kim, B. S. Kim, H. J. Song, H. J. Shin, J. H. Shim, and B. I. Min, Appl. Phys. Lett. **84**, 4233 (2004).

[33] B. T. Thole, P. Carra, F. Sette, and G. van der Laan, Phys. Rev. Lett. **68**, 1943 (1992).

[34] C. T. Chen, Y. U. Idzerda, H.-J. Lin, N. V. Smith, G. Meigs, E. Chaban, G. H. Ho, E. Pellegrin, and F. Sette, Phys. Rev. Lett. **75**, 152 (1995).

[35] J.-S. Kang, G. Kim, H. J. Lee, D. H. Kim, H. S. Kim, J. H. Shim, S. Lee, H. G. Lee, J.-Y. Kim, B. H. Kim, and B. I. Min, Phys. Rev. B **77**, 035121 (2008).

[36] L. Stichauer, A. Mirone, S. Turchini, T. Prosperi, S. Zennaro, N. Zema, F. Lama, R. Pontin, Z. Simsa, Ph. Tailhades, and C. Bonningue, J. Appl. Phys. **90**, 2511 (2001).

[37] B. T. Thole, G. van der Laan, J. C. Fuggle, G. A. Sawatzky, R. C. Karnatak, and J. M. Esteva, Phys. Rev. B **32**, 5107 (1985).

[38] A. Yang, X. Zuo, C. Vittoria, and V. H. Harris, IEEE Trans. Magn. **42**, 2870 (2006).

[39] C. Carvallo, Ph. Sainctavit, M.-A. Arrio, N. Menguy, Y. Wang, G. O.-Nguema, and S. Brice-Profeta, Am. Mineral. **93**, 880885 (2008)